Results in Optics 12 (2023) 100470

Contents lists available at ScienceDirect

Results in Optics

journal homepage: www.sciencedirect.com/journal/results-in-optics

Monolith $Cs_{1-x}Rb_xSnI_3$ perovskite – silicon 2T tandem solar cell using SCAPS-1D

Emmanuel Akoto [a,*], Victor Isahi [a], Victor Odari [b,c], Christopher Maghanga [a,c], Francis Nyongesa [d]

[a] Department of Physical and Biological Sciences, Kabarak University, P.O. Box Private Bag-20157, Kabarak, Kenya
[b] Department of Physics, Masinde Muliro University of Science and Technology, P.O. Box 190-50100, Kakamega, Kenya
[c] Materials Research Society of Kenya, P.O. Box 15653-00503, Nairobi, Kenya
[d] Department of Physics, University of Nairobi, P.O. Box 30197-00100, Nairobi, Kenya

ARTICLE INFO

Keywords:
Tandem solar cells
Silicon
$Cs_{1-x}Rb_xSnI_3$ perovskite
SCAPS-1D

ABSTRACT

Tandem solar cells (TSCs) have gained notoriety by the use of various absorber layers with different bandgaps. The photovoltaic characteristics of $Cs_{1-x}Rb_xSnI_3$ perovskite – silicon TSCs were determined through simulation using the SCAPS-1D software in this work by first validating the experimentally obtained efficiency of 2.08% for ITO/$Cs_{0.8}Rb_{0.2}SnI_3$/PCBM/BCP/Al structure. The influence of chlorinated and undoped ITO front contact, variation of Electron Transport Layer (ETL) thickness, doping concentration, CBO and variation of absorber layer thickness, defect density, and doping concentration was studied. Optimum V_{OC} (0.9893 V), J_{SC} (30.04 mA/cm2), fill factor (81.78 %) and efficiency (24.31 %) were determined. The bottom cell was simulated independently with reference to experimental data using the structure Al/c-Si (n)/c-Si (p)/c-Si (p +)/Au resulting in an efficiency of 26.68 %. The monolithic $Cs_{0.8}Rb_{0.2}SnI_3$ perovskite – silicon tandem solar cell of the architecture ITO/$Cs_{0.8}Rb_{0.2}SnI_3$/c-Si (n)/c-Si (p)/c-Si (p +)/Au performance was analyzed by varying the thickness, doping concentration, and defect density of the active layers. Optimized parameters obtained were as follows: top perovskite layer thickness (100 nm), doping concentrations (5×10^{19} cm^{-3}) and defect density (1×10^{13} cm^{-3}), and bottom silicon absorber layer thickness (50 μm), doping concentrations (5×10^{16} cm^{-3}), defect density (1×10^{12} cm^{-3}), and a work function of 5.3 eV with chlorinated ITO as the front contact of the tandem cell. Optimized outcomes of efficiency (29.82 %), V_{OC} (0.7992 V), J_{SC} density (43.39 mA/cm^2), and fill factor (85.98 %) were realized for the 2T $Cs_{0.8}Rb_{0.2}SnI_3$ perovskite – silicon tandem solar cell.

1. Introduction

Solar power has drawn a lot of attention as a source of sustainable, clean, and green energy in this age of rapidly advancing technology (Saga, 2010). To create effective and affordable solar cells, a tremendous amount of effort has been made. Si-based solar cells have undergone decades of development, including wafer surface treatment, device structure design, Si defects passivation, optical design, and optical design, which gradually increases the device efficiency to a world-record value of 26.1% for single crystal Si cells (Partain et al., 19871987), 23.3% for multi-crystalline Si cells (Richter et al., 2017), and 26.7% for Si-based heterostructure solar cells (Stevenson and Luchkin, 2021). Since the invention of PV, c-Si wafer-based photovoltaic (PV) devices have been successfully developed and commercialized, and dominated the global solar power market (by about 90%) (Fazal and Rubaiee, 2023). The benefits of C-Si solar cells include their ease of production, environmental friendliness, vitality, excellent performance and its ability to withstand adversity. Further advancement in efficiency of the solar cells, becomes a bottleneck, with its efficiency approaching the Shockley-Quisser (S-Q) limit of 29% for a single-junction cell (Stevenson and Luchkin, 2021). This is primarily due to the indirect optical bandgap of the c-Si is c-Si (1.12 eV), as a result of the relatively low optical absorption coefficient of C-Si cells (Saga, 2010), necessitating the relatively thick layer of absorber material. This coupled with the high-purity crystals required (Saga, 2010), and the high processing cost of a c-Si wafer (50% of the manufacturing cost of a c-Si PV module), research on a new module for solar cells becomes necessary.

Perovskite solar cells (PSCs) attracted attention as one of the most

* Corresponding author.
E-mail address: akoto@kabarak.ac.ke (E. Akoto).

https://doi.org/10.1016/j.rio.2023.100470
Received 17 March 2023; Received in revised form 21 May 2023; Accepted 26 June 2023
Available online 28 June 2023

promising photovoltaic (PV) technology (Gan et al., 2020) due to the high light absorption coefficient, long carrier diffusion length, and solution processibility of metal perovskite materials hence the potential for high efficiencies and low manufacturing cost (Hao et al., 2021). Lead-based perovskite solar cells exhibit outstanding performance (Noel et al., 2014). However, Pb toxicity increases environmental damage and is a barrier to the mass production and commercialization of perovskite solar cells. To enhance the affordability of PSCs the Pb-reduced or Pb-free perovskite to became necessary (Jayan, 2023). The lead–free perovskites however are faced with a major challenge of low efficiency and stability. Novel design strategies for perovskite materials with improved stability and high performance have to be explored (Babics et al., 2023; Li et al., 2023). Tin (Sn) has shown the highest PCE among potential low toxicity Pb substitutes (Wei et al., 2016). Several studies have been done on Sn-based perovskites; $FASnI_3$ ($HC(NH_2)_2SnI_3$), $MASnI_3$ ($CH_3NH_3SnI_3$) and $CsSnI_3$. They found that organic-based (FA, MA) perovskites intrinsically had low stability; this led to Cs based cation perovskite to become the favorite candidate (Wu et al., 2017). Tuning of the electronic structure of B-γ- $CsSnI_3$ by substitution of A-site Cs cation with the smaller Rb cation. B- γ- $CsSnI_3$ PV devices with an inverted planar device architecture exhibit the best efficiency and stability without a hole-transport layer. The addition of SnF_2 to Sn- based perovskites has been shown to reduce the oxidation of Sn^{2+} to Sn^{4+} (Minemoto and Murata, 2015). In spite of the progress made in improving performance of Sn-based PSCs, it still has a low PCE.

Tandem solar cells have potential to raise the efficiency past the theoretical limit due to their ability to exploit the sun better (Schulze et al., 2020). Monolithic tandem techniques, first recorded in 2015 have experienced a remarkable development over time, with the PCEs recently improved to 23.5 % (Ruiz-Preciado et al., 2022); 28.7 % (Sveinbjörnsson et al., 2022) and ~ 20 % (Zheng et al., 2022) and for Perovskite – Perovskite – Silicon Triple - Junction, perovskite - silicon and 2T perovskite - CIGS tandems, respectively. In silicon-perovskite tandem device, the high energy and low energy photons are absorbed by the top high band gap (perovskite) and low band gap semiconductor of bottom cell (Silicon) respectively (Zhao et al., 2023). This diminishes the thermalization and optical losses, significant efficiency limiting factors in single junction cells.. The perovskite $Cs_{1-x}Rb_xSnI_3$ with ~ 1.4 eV bandgap is a compatible contender as a material for the top cell (Marshall et al., 2018), hence necessitating the study of $Cs_{1-x}Rb_xSnI_3$ perovskite - Si tandem solar cell. Several attempts to improve the tandem cell include minimizing the parasitic absorption and reflection losses (Bush et al., 2018) by adding MACl and MAH_2PO_2 in the perovskite precursor (Chen et al., 2019). Utilizing a textured foil for light manipulation (Jäger et al., 2019), use of silicon oxide nanocrystalline based optical interlayer in perovskite - silicon tandem solar cell (Mazzarella et al., 2019) and using high temperature resistant p-type crystalline silicon lower cells in 2T perovskite - silicon tandem solar cells (Nogay et al., 2019). Combining rear silicon hetero-junction lower cells with p-i-n perovskite top cells that gave certified PCE of 25% and 26% after reducing current mismatch (Köhnen et al., 2019).

A clear understanding of the relationship between material parameters and device architecture is vital in the improvement of the performance of the $Cs_{1-x}Rb_xSnI_3$ perovskite cell. This study submits conceivable optimization approaches for performance improvement of the $Cs_{1-x}Rb_xSnI_3$ perovskite device with each structure parameter and operating condition intuitively examined (Nalianya et al., 2021). A comprehensive understanding of the complex relationship between the different parameters that affect perovskite solar cell to estimate optimum values for the best performance of the solar cell and the impact of the $Cs_{1-x}Rb_xSnI_3$ perovskite solar cell when in tandem with the already successful silicon solar cell is attempted in this study. We independently developed models for $Cs_{1-x}Rb_xSnI_3$ perovskite and (C-Si) and hence a monolithic Pero - Si tandem solar cell. The respective cells were optimized, and their performance studied by varying prime parameters. We also analyzed and compared the performance of the simulated structures with some experimental results. The fabrication techniques used for each cell (both perovskite and silicon), and a possible alignment considering the recent advancements and engineering (Babics et al., 2023; Zhao et al., 2023) in 2T Tandem solar cells is highlighted. The whole research study was carried out with the solar capacitance simulation (SCAPS 1D) software.

2. Materials and methods

2.1. Simulation of $Cs_{1-x}Rb_xSnI_3$ perovskite solar cell

SCAPS-1D (ver.3.3.03) software was used for the device modelling. Various panels of the software are used to set or adjust the parameters from which results are inferred. In two-band gap system, higher bandgap absorber material forms the upper cell and lower bandgap absorber material forms the lower cell for optimum operation (Bremner et al., 2016). Perovskite bandgap energies range from 1.4 eV to 1.9 eV (larger than silicon, band gap of ~ 1.1 eV). This is relevant to the upper active layer for an efficient 2-band gap structure (Almansouri et al., 2015). SCAPS is fundamentally based on Poisson's differential equation for electrons and holes of semiconductors described in equation (1), coupled continuity differential equations and carrier transport equations in equation (2) and (3) below solved by Newton-Raphson and Gummel type iteration method.

$$\frac{d}{dx}\left(\epsilon[x]\frac{d\varphi}{dx}\right) = q[p(x) - n(x) + N_{d^+}(x) - N_{a^-}(x) + p_t(x) - n_t(x)] \quad (1)$$

$$\frac{dp_n}{dt} = G_P - \frac{p_n - p_{no}}{\tau_p} - p_n u_p \frac{dE}{dx} - u_p E \frac{dp_n}{dx} + D_P \frac{d^2 p_n}{dx^2} \quad (2)$$

$$\frac{dn_p}{dt} = G_n - \frac{n_p - n_{po}}{\tau_n} - n_p u_n \frac{dE}{dx} - u_n E \frac{dn_p}{dx} + D_n \frac{d^2 n_p}{dx^2} \quad (3)$$

The perovskite solar cell's architecture is an inverted heterojunction of ITO/$Cs_{1-x}Rb_xSnI_3$/PCBM/BCP/Al as shown in Fig. 1 (a) with its energy band diagram in Fig. 2 (a), has a reported a PCE of 2.08 % experimentally (Marshall et al., 2018). Validation of results was accomplished by comparison of the simulated and experimental inverted (p-i-n) architecture of ITO(p)/$Cs_{1-x}Rb_xSnI_3$ (i)/PCBM (n)/BCP/Al. A numerical variation of band gap with varying molar composition × in $Cs_xRb_{1-x}SnI_3$ was done to study the behavior of the band gap in the perovskite material. The CBO sign can be positive or negative contingent upon the

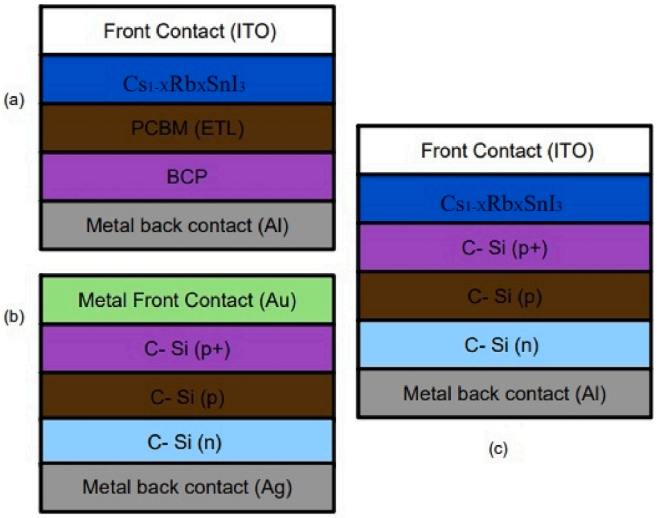

Fig. 1. Solar cells architecture, (a) p-i-n architecture of ITO/$Cs_{1-x}Rb_xSnI_3$/PCBM/BCP/Al, (b) Single junction Si cell of c-Si (p +)/c-Si (p)/c-Si (n) architecture and (c) $Cs_{1-x}Rb_xSnI_3$ – Si Tandem Solar cell Structure.

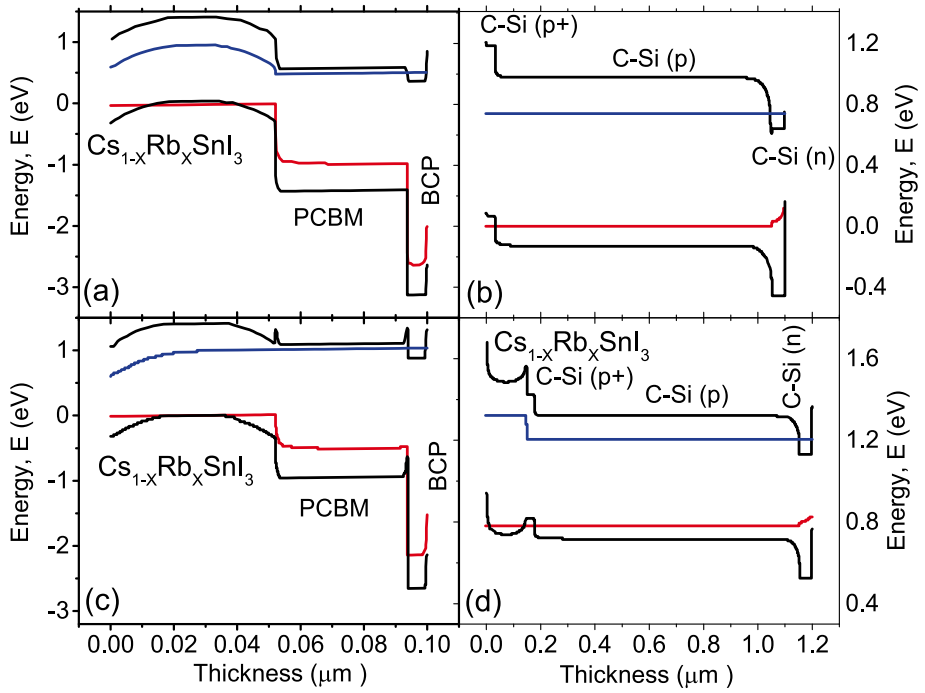

Fig. 2. Energy band diagrams of (a) $Cs_{1-x}Rb_xSnI_3$ perovskite solar cell with −0.28 eV CBO, (b) Silicon cell with C-Si (p) at 1 μm and (c) $Cs_{1-x}Rb_xSnI_3$ perovskite solar cell with + 0.22 eV CBO (d) $Cs_{1-x}Rb_xSnI_3$ perovskite - Silicon tandem solar cell with C-Si (p) at 1 μm.

photograph created transporter boundary levels as shown in the formulae CBO = (χ_{per} - χ_{ETL}) (Nalianya et al., 2021). To prevent charge recombination at the interface between the absorber and the ETL and to facilitate effective carrier extraction, the CBO should be properly tuned (Nalianya et al., 2021). The (Baloch et al., 2018; Baloch et al., 2018)-Phenyl-C61-butyric acid methyl ester (PCBM) was utilized as the ETL, and its electron affinity varied to obtain the desired CBO. Optimization of absorber thickness, defect density, and doping concentration, ETL (PCBM) thickness, doping concentration and CBO and ITO front contact was done by variation of parameters on specific ranges. Absorber thickness on a range (100 nm – 500 nm), defect density (10^{14} – 10^{17} cm^{-3}) and absorber doping concentration (5×10^{15} cm^{-3} – 5×10^{20} cm^{-3}). ETL (PCBM) thickness on a range (40 nm- 100 nm), doping concentration (1×10^{16}–1×10^{21}) and CBO (- 0.28 eV - +0.22 eV). Influences of the work function of the undoped ITO and Cl - doped ITO on the $Cs_{1-x}Rb_xSnI_3$ perovskite solar cells was varied from 4.7 eV to 5.6 eV. The work function of the Al metal back contact was determined as 4.2 eV.

2.2. Simulation of $Cs_{1-x}Rb_xSnI_3$ –Si tandem structure

A monolithic 2T tandem structure was created by layering a single silicon cell with the $Cs_{1-x}Rb_xSnI_3$ perovskite cell and connecting the two in series. The tandem cell structure of ITO/Perovskite/c-Si (p +)/c-Si (p)/c-Si (n)/Al had $Cs_{1-x}Rb_xSnI_3$ as the top absorber cell and c-Si (p) served as the bottom cell, as shown in Fig. 1 (c), and its energy band diagram in Fig. 2 (c). The n-p-p + structure spans a wide range of light spectrum. The single silicon cell was simulated following experimental data (Jahangir et al., 2021; Yoshikawa et al., 2017) as shown in Fig. 1 (b) with its energy band diagram in Fig. 2 (b). For the optimum performance of the top and base cells' solar-powered pair, a few real characteristics were adjusted, including the thickness, giver/acceptor concentration, and defect density of the absorber layers.

2.3. Device simulation parameters

According to stated experimental data and theoretical studies in literature, all input parameters for simulation were carefully selected. The individual materials parameters for c-Si, $Cs_{0.8}Rb_{0.2}SnI_3$ and $Cs_{0.8}Rb_{0.2}SnI_3$ - C- Si tandem solar cells are shown in Tables 1, 2, 3 and 4. Thermal velocities for electrons and holes were calibrated to10^7 cm/s (Mandadapu et al., 2017) Shunt and series resistance values weren't taken into account, however the model did use the normal AM1.5G spectrum and an operating temperature of 300 K.

3. Results and discussion

3.1. Simulation of the perovskite layer

3.1.1. Validation of results

Comparing simulated performance to experimental device performance demonstrates the veracity of the SCAPS-1D software simulation, as reported by Marshall et al (Marshall et al., 2018) (Table 5). Yoshikawa et al experimental data is also used to simulate a single silicon cell (Yoshikawa et al., 2017); (Jahangir et al., 2021) The calibration findings

Table 1
Simulation Parameters for $Cs_{1-x}Rb_xSnI_3$ Perovskite Solar Cell.

Parameter	Units	BCP	PCBM	$Cs_{0.8}Rb_{0.2}SnI_3$
E_g (Band gap)	eV	3.5 [a]	2.0 [a]	1.4[b]
χ_e (Electron affinity)	eV	3.7 [a]	3.9 [a]	3.62[c]
d (Thickness)	nm	6 [a]	40 [a]	50[b]
ε_r (Permittivity)		10 [a]	4.0 [a]	25.7[c]
μ_n (electron mobility)	cm^2/Vs	2×10^{-2} [a]	1×10^{-1} [a]	5.85×10^{2} [c]
μ_p (hole mobility)	cm^2/Vs	2×10^{-3} [a]	1.5×10^{-2} [a]	4.0×10^{1}[c]
N_C (Effective density of states in the conduction band)	cm^{-3}	1.8×10^{21} [a]	1.8×10^{21} [a]	1.58×10^{19} [c]
N_V (Effective density of states in the valence band)	cm^{-3}	2.2×10^{21} [a]	2.2×10^{21} [a]	1.47×10^{18} [c]
N_A (Carrier density of the acceptor)	cm^{-3}	1×10^{10} [a]	1×10^{13} [a]	0
N_D (Carrier density of the donor)	cm^{-3}	1×10^{21}	1×10^{18}	5×10^{18}

Table 2
Simulation Parameters for $Cs_{0.8}Rb_{0.2}SnI_3$ - C- Si Tandem Solar Cell Parameters.

Parameter	Units	$Cs_{0.8}Rb_{0.2}SnI_3$	c-Si (n)	c-Si (p)	c-Si (p +)
E_g (Band gap)	eV	1.4[b]	1.124 [d]	1.124 [d]	1.124 [d]
χ_e (Electron affinity)	eV	3.62[c]	3.9 [d]	4.05 [d]	3.9 [d]
d (Thickness)	nm	150[b]	50 nm [d]	100 μm [d]	30 nm [d]
ε_r (Permittivity)		25.7[c]	11.9 [d]	11.9 [d]	11.9 [d]
μ_n (electron mobility)	cm^2/Vs	5.85×10^{2} [c]	1250 [d]	1010 [d]	1212 [d]
μ_p (hole mobility)	cm^2/Vs	4.0×10^{1}[c]	443 [d]	443 [d]	421 [d]
N_C (Effective density of states in the conduction band)	cm^{-3}	1.58×10^{19} [c]	2.8×10^{19} [d]	2.8×10^{19} [d]	2.84×10^{19} [d]
N_V (Effective density of states in the valence band)	cm^{-3}	1.47×10^{18} [c]	1.04×10^{19} [d]	1.04×10^{19} [d]	1.04×10^{19} [d]
N_A (Carrier density of the acceptor)	cm^{-3}	0	0	5×10^{16}	9.5×10^{18} [d]
N_D (Carrier density of the donor)	cm^{-3}	5×10^{15}	8×10^{21}	0	0

are well matched to the experimental data (Marshall et al., 2018), proving the accuracy and viability of our simulation's device setup and material characteristics as shown in Table 6. Fig. 3 (a) shows that increasing the Rb substitution (x) increases the band gap (E_g) in $Cs_{1-x}Rb_xSnI_3$. DFT-1/2 is used to compute this band gap. DFT calculations have an uncertainty of about 0.1 eV. This increase is attributed to the distortion of the SnI_6 octahedral lattice that happens when Cs is replaced with Rb, yet it also lessens the stability against disintegration (Marshall et al., 2018). The ideal value of ×, where the stability is enough for usage as the light-harvesting layer in inverted photovoltaic (PV) devices, was found at 0.2 by varying the molar composition of Cesium (Cs) and Rubidium (Rb). Fig. 3(b) is a validity test to the viability of SCAPS 1D to simulate predict the patterns of $Cs_{0.8}Rb_{0.2}SnI_3$ perovskite material that is being tested for photovoltaic application in order to optimize its parameters. Comparing device performance from actual experimental characterization reported in literature, the SCAPS device simulation's validity is demonstrated. (Marshall et al., 2018).

3.1.2. Effect of thickness (nm) and defect density, N_T (cm^{-3}) absorber layer on photovoltaic characteristics of $Cs_{1-x}Rb_xSnI_3$ perovskite solar cell

The PCE of various defect density (1×10^{14} cm^{-3} to 1×10^{17} cm^{-3}) with increasing absorber thickness was simulated to obtain optimum defect density as demonstrated in Fig. 4. Absorber thickness is thereafter varied from 100 nm to 500 nm at optimum defect density of the $Cs_{0.8}Rb_{0.2}SnI_3$ perovskite absorber layer to determine their effects on the solar cell performance. The optimum value of trap density is determined at 1×10^{15} cm^{-3} (diffusion length of 640 nm). The thickness of $Cs_{0.8}Rb_{0.2}SnI_3$ perovskite layer is then varied from 50 nm to 500 nm at optimum defect density. Increase in $Cs_{0.8}Rb_{0.2}SnI_3$ perovskite layer thickness leads to an increase in solar cell PCE from 2.08 % at 50 nm, peaks at 200 nm (3.04 %) and thereafter deteriorates to 2.34 % at 500 nm. The J_{sc}, similar to the PCE increases from 6.63 mA/cm^2 at 50 nm, peaks at 8.82 mA/cm^2 at 200 nm and thereafter significantly reduces to 6.85 mA/cm^2 at 500 nm. The V_{oc} also increases from 0.4757 V at 50 nm, peaks at 0.4901 V at 200 nm and thereafter reduces to 0.4807 at 500 nm with increasing absorber thickness. The FF increases from 65.97 % at 50 nm and increases to a maximum value of 71.14 % at 500 nm. The preferred optimized thickness for the $Cs_{0.8}Rb_{0.2}SnI_3$ perovskite based solar cell is selected at 200 nm, within the diffusion length range. The increase in thickness of the absorber layer leads to an increase in the effective bandgap, which consequently results in the increase of the *Voc.* Due to increased recombination loss, the Voc suddenly drops for the photoactive layer that is thicker than the ideal thickness (Bag et al., 2020; Nalianya et al., 2021). More defects per unit of area leads to a reduction in the photocurrent hence increasing the number of trap centers. The PCE increases for $N_T = 1 \times 10^{15}$ cm^{-3} due to increased exciton generation due to increased exciton generation due to higher absorption as the absorber thickness rose (Nalianya et al., 2021) peaking at 200 nm. The FF increases significantly. implying that the FF is related to the efficiency of charge extraction that resulted from smaller built in voltage in the thicker devices (Momblona et al., 2014), meaning, increasing thickness increases the photon-capturing ability, which results in an increase in the rate of generation of charge carriers (Rai et al., 2020).

Table 4
Interface properties in $Cs_{0.8}Rb_{0.2}SnI_3$ Perovskite solar cell and $Cs_{0.8}Rb_{0.2}SnI_3$ - C-Si Tandem solar cells.

		Interface	PCBM/ $Cs_{0.8}Rb_{0.2}SnI_3$	$Cs_{0.8}Rb_{0.2}SnI_3$/C-Si (p)
Parameter		Type	Neutral	Neutral
Density of defects		cm^{-2}	1×10^{12}	1×10^{12}
Capture cross-section	Electron (σ_n)	cm^{-2}	1×10^{-10}	1×10^{-10}
	Holes (σ_p)	cm^{-2}	1×10^{-10}	1×10^{-10}
Energy		E_V	Below the lowest E_C	Below the lowest E_C

a. (Moiz and Alahmadi, 2021) b. (Marshall et al., 2018) c. (Jahangir et al., 2021) d. (Lin et al., 2021).

Table 5
ITO/$Cs_{0.8}Rb_{0.2}SnI_3$/PCBM/BCP/Al perovskite solar cell architecture.

	V_{oc} (V)	J_{sc} (mA/cm^2)	FF (%)	PCE (%)
Experimental (Marshall et al., 2018)	0.50 ± 0.01	6.71 ± 0.71	0.61 ± 0.03	2.05 ± 0.26
SCAPS 1D	0.4757	6.63	0.6597	2.08

Table 6
Au/c-Si (p +)/c-Si (p)/c-Si (n)/Al silicon solar cell architecture.

	V_{oc} (V)	J_{sc} (mA/cm^2)	FF (%)	PCE (%)
EXPERIMENT (Aman et al., 2021; Yoshikawa et al., 2017)	0.744	42.3	83.8	26.3 ± 0.5
SCAPS FILE	0.7443	43.29	83.30	26.68

Table 3
Defects properties in $Cs_{0.8}Rb_{0.2}SnI_3$ Perovskite solar cell and $Cs_{0.8}Rb_{0.2}SnI_3$ - C- Si Tandem solar cells.

		Units	BCP	PCBM	$Cs_{0.8}Rb_{0.2}SnI_3$	c-Si (n)	c-Si (p)	c-Si (p +)
Type			Neutral	Neutral	Neutral	Neutral	Neutral	Neutral
Density of defects		cm^{-3}	1×10^{17}	1×10^{14}	10^{10} to10^{19}	1×10^{12}	1×10^{12}	1×10^{12}
Capture cross section	Electron (σ_n)	cm^2	1×10^{-15}	1×10^{-14}	1×10^{-15}	1×10^{-17}	1×10^{-17}	1×10^{-17}
	Holes (σ_p)	cm^2	1×10^{-17}	1×10^{-14}	1×10^{-15}	1×10^{-17}	1×10^{-17}	1×10^{-17}
Energy		eV	Above E_V	Above E_V	Above E_V	Above E_V	Above E_V	Above E_V

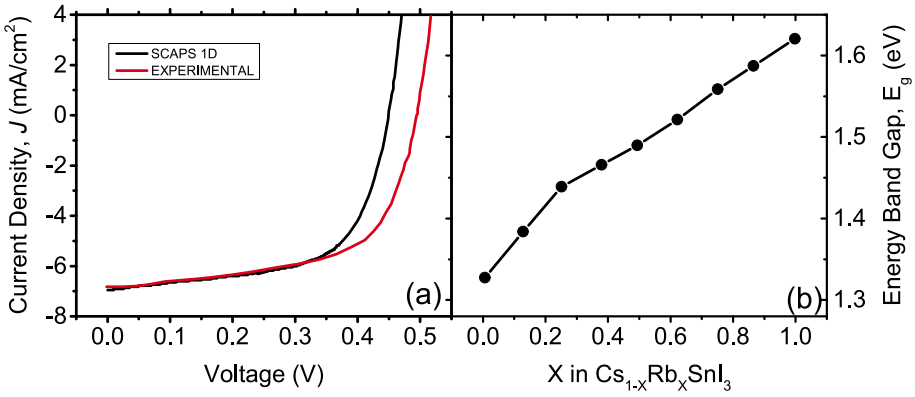

Fig. 3. (a) Experimental (Marshall et al., 2018) and Simulation Graphs of $Cs_{0.5}Rb_{0.5}SnI_3$ (b) Band gap evolution of $Cs_{1-x}Rb_xSnI_3$ with increasing Rb (x) substitution (Marshall et al., 2018).

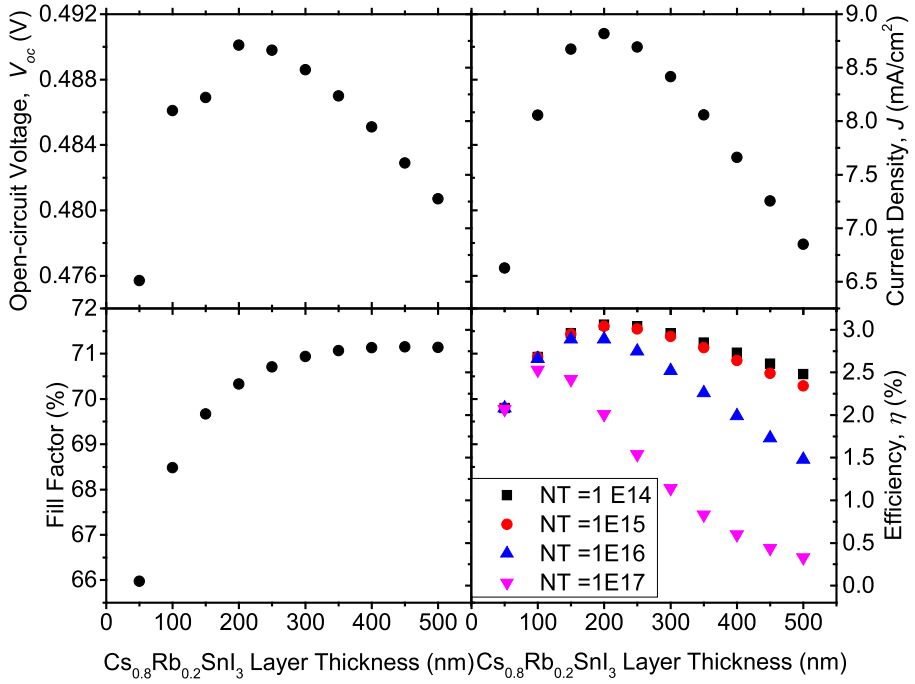

Fig. 4. Effect of thickness (nm) and defect density, N_T (cm^{-3}) absorber layer on photovoltaic characteristics of $Cs_{1-x}Rb_xSnI_3$ perovskite solar cell.

3.1.3. Effect of absorber doping concentration on solar cell parameters of $Cs_{1-x}Rb_xSnI_3$ perovskite solar cell

To understand the influence of absorber doping concentration on solar cell charachteristics of $Cs_{0.8}Rb_{0.2}SnI_3$ perovskite solar cell, doping levels (N_D) varied from 5×10^{15} cm^{-3} to 5×10^{20} cm^{-3} as shown in Fig. 5. The PCE, similar to the FF decrease with the increasing N_A values to minimum values of 2.08 % at 5×10^{18} cm^{-3} and 61.83 % at 5×10^{17} cm^{-3} respectively and thereafter increase slightly. The V_{oc} increases from 0.6748 V at 5×10^{15} cm^{-3}, decreases drastically to a minimum value of 0.4757 V at 10^{18} cm^{-3} and thereafter improves to 0.7261 V at 5×10^{20} cm^{-3}. However, J_{sc} decreases from 11.05 mA/cm^2 at 5×10^{15} cm^{-3} to 5.98 mA/cm^2 at 5×10^{20} cm^{-3}. The decline in the ratio of charge carrier production to recombination rates in the major regions of the photoactive layer is what is responsible for the reduction in Jsc (Nalianya et al., 2021). The FF declines with increasing doping concentration since there is increase in series resistance in the cell. The FF varies monotonically with the PCE hence the similar pattern of behavior. The V_{oc} increases due to increased share of radiative recombination at open-circuit condition. The optimal efficiency is deduced, showing that charge carriers are efficiently gathered and transferred at $N_A = 5 \times 10^{15}$ cm^{-3}. Fig. 6 shows different J-V Spectra with increasing doping concentrations of $Cs_{0.8}Rb_{0.2}SnI_3$ absorber layer.

3.1.4. Effect of electron transport layer, ETL (PCBM) thickness, doping concentration and conduction band Offset (CBO) on $Cs_{1-x}Rb_xSnI_3$ perovskite solar cell parameters

3.1.4.1. Electron transport layer, ETL (PCBM) thickness. In Fig. 7 below, the effect of ETL (PCBM) thickness on the device performance is demonstrated. The V_{oc}, J_{sc}, FF and PCE are shown to increase significantly with increasing PCBM thickness. The ETL (PCBM) thickness is varied from 20 nm to 100 nm. The V_{oc} increases from 0.47 V at 20 nm to 0.48 V at 100 nm. The J_{sc} increases from 5.98 mA/cm^2 at 20 nm to 7.29 mA/cm^2 at 100 nm. The PCE increases from 1.48 % at 20 nm to 2.32 % at 100 nm. The FF increases from 65.48 % at 20 nm to 66.36 % at 100 nm. The rise in V_{oc} is attributable to low recombination due to efficient charge carrier separation at the PCBM/$Cs_{0.8}Rb_{0.2}SnI_3$ interface. The increase in J_{sc} could be due to an increase in light transmittance through

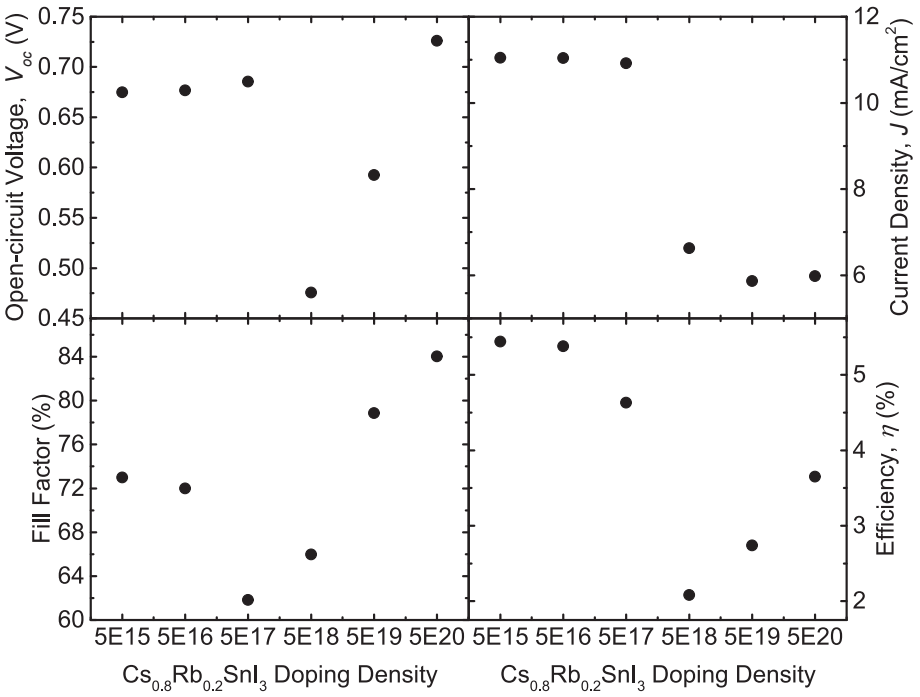

Fig. 5. Effect of absorber doping concentration on solar cell parameters of $Cs_{1-x}Rb_xSnI_3$ perovskite solar cell.

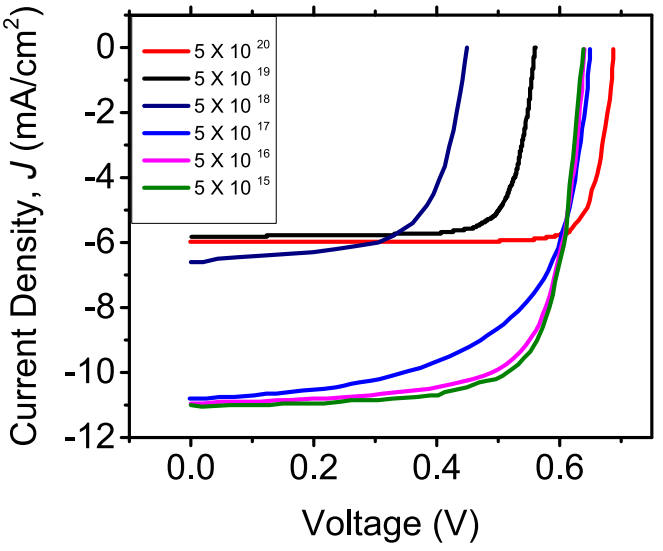

Fig. 6. J-V Spectra with increasing doping concentrations of $Cs_{0.8}Rb_{0.2}SnI_3$ absorber layer.

the thicker ETL layer. Due to a drop in the device's series resistance, the FF increases as PCBM thickness increases. The 100 nm PCBM layer in the perovskite exhibits the best performance and hence optimum ETL thickness in this study.

3.1.4.2. Electron transport layer, ETL doping concentration. In Fig. 8 below, the V_{oc}, J_{sc}, FF and PCE are shown to eventually increase significantly with the ETL layer's increasing doping level despite initial variations. The doping concertation of the ETL (PCBM) layer is varied from 1×10^{16} cm^{-3} to 1×10^{21} cm^{-3}. The J_{sc} increases from 3.91 mA/cm^2 at 1×10^{16} cm^{-3} to 7.33 mA/cm^2 at 1×10^{21} cm^{-3}. The PCE increases from 1.72 % at 1×10^{16} cm^{-3} to a maximum value of 3.72 % at 1×10^{21} cm^{-3}. The FF first increases from 69.80 % at 1×10^{16} cm^{-3}, peaks at 77.51 % at 1×10^{18} cm^{-3}, decreases to 65.97 % at 1×10^{20} cm^{-3} and finally increases to 70.19 % at 1×10^{21} cm^{-3}. The V_{oc} first decreases from 0.63 V at 1×10^{16} cm^{-3} to a minimum value of 0.46 V at 1×10^{20} cm^{-3} and leaps to 0.72 V at 1×10^{21} cm^{-3}.There is increased FF due to decreasing series resistance with increased doping. There is a steep increase in the V_{oc} with decreasing recombination rate at the bulk of the absorber (Agha and Algwari, 2021). With increased doping, there is an increasingly strong built-in electric field across the device (Bag et al., 2020) facilitating efficient separation of carriers hence an increase in the J_{sc} and eventually the PCE. The optimal PCE (3.72 %) corresponds to a high doping concentration at 1×10^{21} cm^{-3} which is determined to be the optimal doping concentration.

3.1.4.3. Electron transport layer, ETL CBO. Electrical and optical characteristics of (Baloch et al., 2018; Baloch et al., 2018)-Phenyl-C61-butyric acid methyl ester (PCBM) was used as ETL and its electron affinity varied to get the intended CBO. Fig. 6 shows the energy band diagram for the perovskite solar cell with (a) – 0.28 eV and (b) + 0.22 eV CBO of the ETL/Absorber interface. The photo generated electron flow towards the metal back contact and are not interrupted when the CBO is increasingly positive. Growing negative CBO impedes the flow of photogenerated electrons toward the metal back contact, leading in a decrease in PCE (Nalianya et al., 2021; Scharber et al., 2006). With enhanced electron and hole accumulation for high defect density at the interface, negative CBO promotes interface recombination and causes poor charge output, as illustrated in Fig. 9 (PCE against CBO for interface densities 10^{12} cm^{-3} and 10^{15} cm^{-3}). Interface defect concentrations have a significant impact on both PCE and current density. The CBO does not however appear to have a substantial impact on current density as demonstrated in Fig. 9. Due to increased carrier density primarily affecting carrier recombination at the ETL/Absorber, a positive CBO with few interface flaws is preferred for better cell performance. The conduction band of the ETL is hence best positioned below the matching photoactive absorber bands, as shown at + 0.22 eV.

3.1.5. Effect of different work functions of front contact of $Cs_{1-x}Rb_xSnI_3$ perovskite solar cell parameters

Chlorinated ITO (Cl: ITO) are reported to have high WF in the range of 4.9 eV – 5.6 eV (Rahman et al., 2020) which suit the high fermi levels

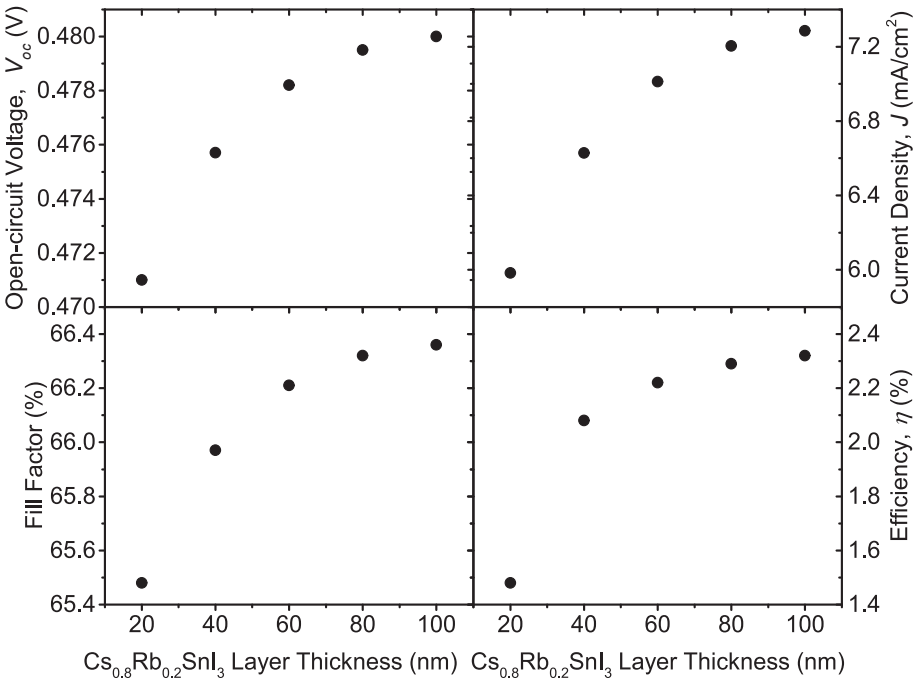

Fig. 7. Effect of Electron Transport Layer, ETL (PCBM) Thickness on $Cs_{1-x}Rb_xSnI_3$ perovskite solar cell parameters.

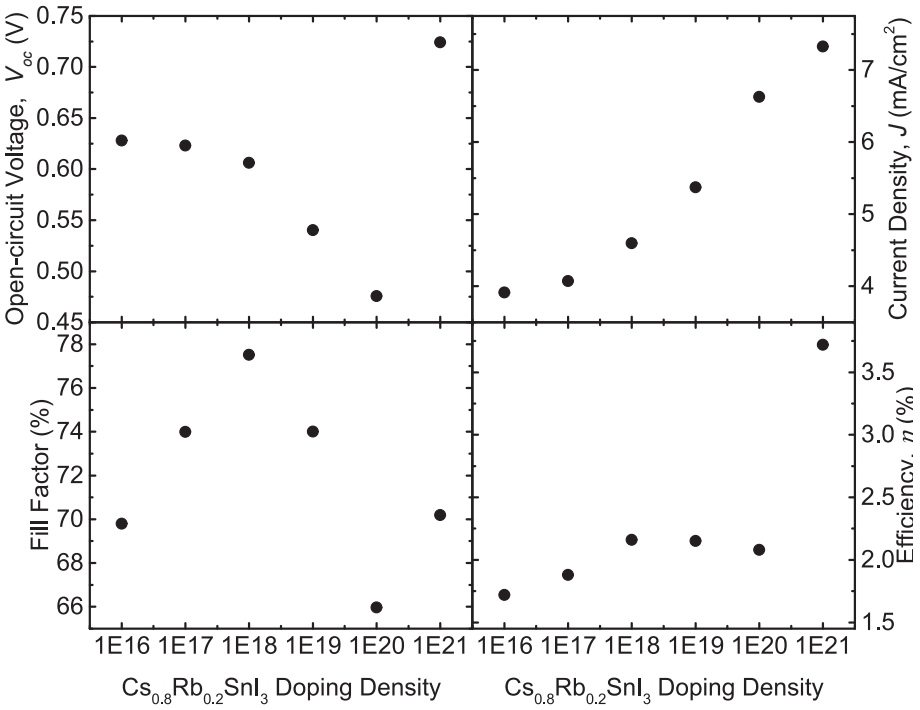

Fig. 8. Effect of Electron Transport Layer, ETL (PCBM) Doping Concentration on $Cs_{1-x}Rb_xSnI_3$ perovskite solar cell parameters.

of perovskites without a HTL layer. The V_{oc} increased steadily from 0.4757 V at 4.7 eV to 0.5018 at 5.3 eV. The J_{sc} increased from 6.63 mA/cm^2 at 4.7 eV to 11.24 mA/cm^2 at 5.3 eV. The FF increases from 65.97 % at 4.5 eV to 72.54 % at 5.3 eV. The PCE increases from 2.08 eV to 4.09 % at 5.3 eV. All the parameters levels off with increasing work function until 5.6 eV after attaining a maximum at 5.3 eV as demonstrated in Fig. 10. A high conductive path is produced by ITO's high work function (Zhang et al., 2014) for carrier extraction, which reduced series resistance in the cell and increased the device's FF. Increases are made to the device's built-in potential (V_{bi}), which controls exciton dissociation and sets the upper bound on the achievable V_{oc} (Zhang et al., 2014) with increasing work function hence the increasing V_{oc} values. Increase in work function subsequently leads to the better energy alignment hence better carrier extraction necessitating the increase in J_{sc} values. The optimum ITO work function is selected at 5.3 eV since a considerably simpler device construction is made possible by high work function hence the improved PCE in the device.

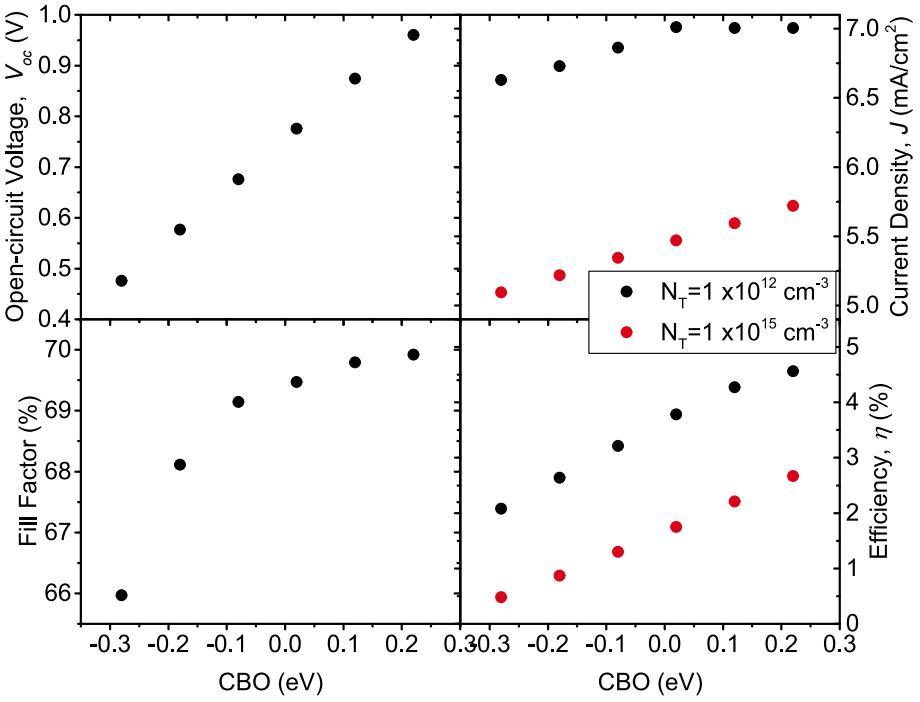

Fig. 9. Effect of Electron Transport Layer Conduction Band Offset (CBO) on $Cs_{1-x}Rb_xSnI_3$ perovskite solar cell parameters.

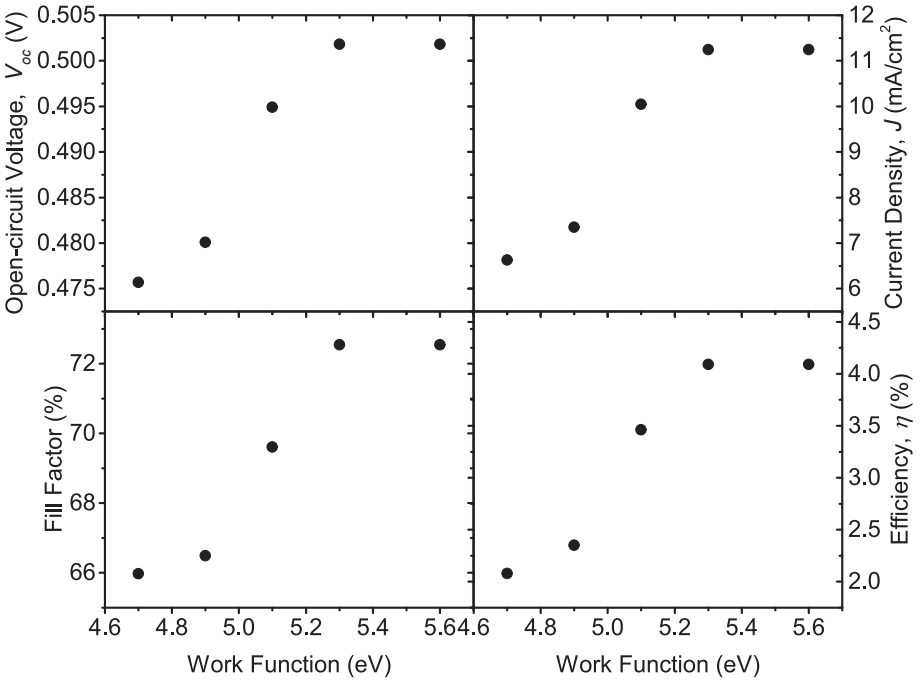

Fig. 10. Effect of Different work functions of front contact of $Cs_{1-x}Rb_xSnI_3$ perovskite solar cell parameters.

3.2. Monolithic $Cs_{1-x}Rb_xSnI_3$ perovskite – silicon 2T tandem solar cell

Tandem solar cells exploit sunlight better (Cheng and Ding, 2021). A perovskite cell is added on top of a single-junction silicon solar cell to produce a 2T tandem structure that traps long solar radiation wavelengths (Aman et al., 2021). The structure utilizes a top cell with a bandgap that is greater than silicon's bandgap of 1.124 eV. The perovskite $Cs_{1-x}Rb_xSnI_3$ with ~ 1.4 eV bandgap is a compatible contender as a material for the top cell in tandem configuration (Marshall et al., 2018). Due to the possibility of increasing efficiency, past the S-Q theoretical limit (Baloch et al., 2018), silicon - perovskite tandem solar cells structure are a dependable alternative. This study investigated the effects of absorber thickness, doping level, and defect density of each absorber layer in detail.

3.2.1. Effect of perovskite thickness variation in $Cs_{1-x}Rb_xSnI_3$ perovskite - silicon tandem solar cell

The thickness of $Cs_{1-x}Rb_xSnI_3$ perovskite absorber layer was varied from 100 nm to 1 μm to determine its influence on the $Cs_{1-x}Rb_xSnI_3$ perovskite - Si tandem solar cell in Fig. 11. The FF decreases with

increasing perovskite thickness from 85.86 % at 100 nm to 85.46 % at 1 μm. The V_{oc} slightly decreases from 0.79 V at 100 nm to 0.76 V at 1 μm with increasing thickness of the perovskite layer. The J_{sc} decreases drastically from 42. 74 mA/cm^2 at 100 nm to 14.23 mA/cm^2 at 1 μm. The PCE decreases from 28.86 % at 100 nm to 9.22 % at 1 μm. The decrease in FF suggests an increase in series resistance with increasing perovskite absorber thickness in the cell. The decrease in V_{oc} is a measure of reduced exciton dissociation with increasing perovskite thickness (Scharber et al., 2006). The decrease in J_{sc} is due to increased carrier combination rate versus the carrier generation rate with increasing absorber thickness. The reduced exciton dissociation therefore reduce the carriers, increases recombination and hence decreases the efficiency (Duan et al., 2020). Optimum perovskite thickness is realized at 100 nm which gives the highest efficiency (28.86 %).

3.2.2. *Effect of silicon c-Si (p) thickness variation in $Cs_{1-x}Rb_xSnI_3$ perovskite- silicon tandem solar cell*

The c-Si (p) absorber layer thickness was varied from 50 μm to 400 μm to investigate the effect of the silicon absorber in the tandem solar cell. In Fig. 12, increase in the active layer thickness leads to a decrease in the V_{oc}, J_{sc}, FF and PCE in the solar cell. The J_{sc} of the device decreases from 41.04 mA/cm^2 at 50 μm to 40.42 mA/cm^2 at 400 μm. The V_{oc} values decrease from 0.79 V at 50 μm to 0.78 V at 400 μm with increasing thickness. The FF values decrease slightly from 85.87 % at 50 μm to 85.67 % at 400 μm. The PCE values decrease slightly from 27.70 % at 50 μm to 27.12 at 400 μm with increasing c-Si (p) thickness. The V_{oc} decreases due to increased recombination in the thicker absorber layers. There is increased series resistance in the active layer with increasing thickness hence the dwindling values of FF. The decreasing J_{sc} points to a decrease in spectral response at the longer wavelength solar irradiance (Nalianya et al., 2021). Larger thicknesses reduce the charge collection while the photo absorption is constant thus reducing the efficiency of the cell (Melas-Kyriazi et al., 2011). Optimum silicon cell thickness is therefore determined at 100 μm.

3.2.3. *Doping concentration (N_D) of perovskite absorber layer in $Cs_{1-x}Rb_xSnI_3$ perovskite- silicon tandem solar cell*

The doping concentration (N_D) of perovskite Absorber layer was varied from 5 × 10^{15} cm^{-3} to 5 × 10^{20} cm^{-3} to determine the effect of doping the perovskite layer on the photovoltaic characteristics of the tandem solar cell. In Fig. 13 all the photovoltaic characteristics J_{sc}, V_{oc}, FF and PCE increase with increasing doping concentration of the perovskite absorber layer. The J_{sc} values increased from 40.99 mA/cm^2 at 5 × 10^{15} cm^{-3}, peaks at 42.96 mA/cm^2 at 5 × 10 ^{18} cm^{-3}, and thereafter decreases to 40.85 mA/cm^2 at 5 × 10^{20} cm^{-3}. The V_{oc} values increased from 0.78 V at 5 × 10^{15} cm^{-3} to 0.80 V at 5 × 10^{20} cm^{-3} with increasing doping concentration. The FF increases from 85.84 % at 5 × 10^{15} cm^{-3} to 85.97 at 5 × 10^{20} cm^{-3}. The PCE increases from 27.64 % at 5 × 10^{15} cm^{-3}, peaks at 5 × 10^{19} cm^{-3} (29.37 %), and sharply drops to 28.18 % at 5 × 10^{20} cm^{-3}. There is an increase in the built voltage, V_{bi} with increasing doping concentration which causes an increase in J_{sc} following the introduction of the majority carriers in the perovskite layer. With the increase in the saturation current of the device, there is increase in the concentration of the acceptor and as a result increasing the V_{oc} (Zhong et al., 2014). The dwindling series resistance attributed to the rise in FF in the cell. The optimum perovskite doping concentration is determined at 5 × 10^{19} cm^{-3} since it yields the maximum PCE (29.37 %) in the solar cell.

3.2.4. *Doping concentration (N_D) of silicon absorber layer in $Cs_{1-x}Rb_xSnI_3$ perovskite- silicon tandem solar cell*

Doping concentration (N_D) of Silicon Absorber layer is varied from 5 × 10^{15} cm^{-3} to 5 × 10^{20} cm^{-3} in to evaluate the effect of doing the crystalline silicon absorber layer on the photovoltaic characteristics of the tandem solar cell. In Fig. 14 the J_{sc} decreases while the V_{oc}, FF and PCE first increase, peak and thereafter decrease with increasing doping levels in the perovskite absorber layer. The J_{sc} values decreased from 41.13 mA/cm^2 at 5 × 10^{15} cm^{-3} to 1.66 mA/cm^2 at 5 × 10^{20} cm^{-3}. The V_{oc} values increased from 0.7852 V at 5 × 10^{15} cm^{-3}, peaks at 5 × 10^{17} cm^{-3} (0.7858 V) and thereafter decrease to 0.7221 V at 5 × 10^{20} cm^{-3} with increasing doping concentration. The FF increases from 85.32 % at 5 × 10^{15} cm^{-3}, peaks at 5 × 10^{17} cm^{-3} (85.89 %) and thereafter decrease to 84.87 % at 5 × 10^{20} cm^{-3}. The PCE slightly increases from 27.56 % at 5 × 10^{15} cm^{-3}, peaks at 5 × 10^{16} cm^{-3} (27.64 %) and sharply drops to 1.02 % at 5 × 10^{20} cm^{-3}. Higher carrier density enhances the recombination process, reducing the likelihood of collecting electrons

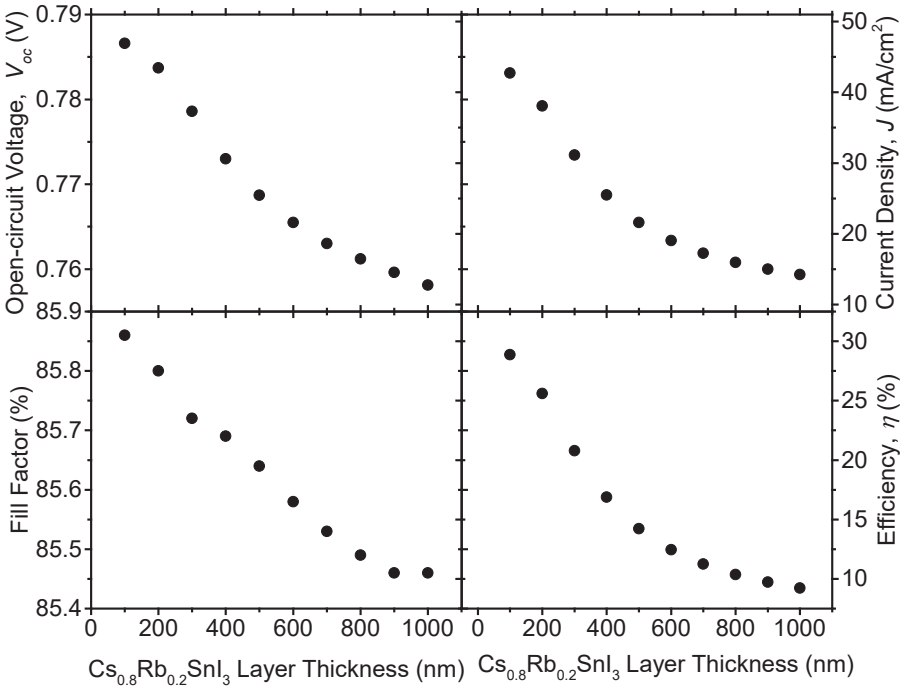

Fig. 11. Effect of Perovskite thickness variation in $Cs_{1-x}Rb_xSnI_3$ perovskite- Silicon Tandem Solar Cell.

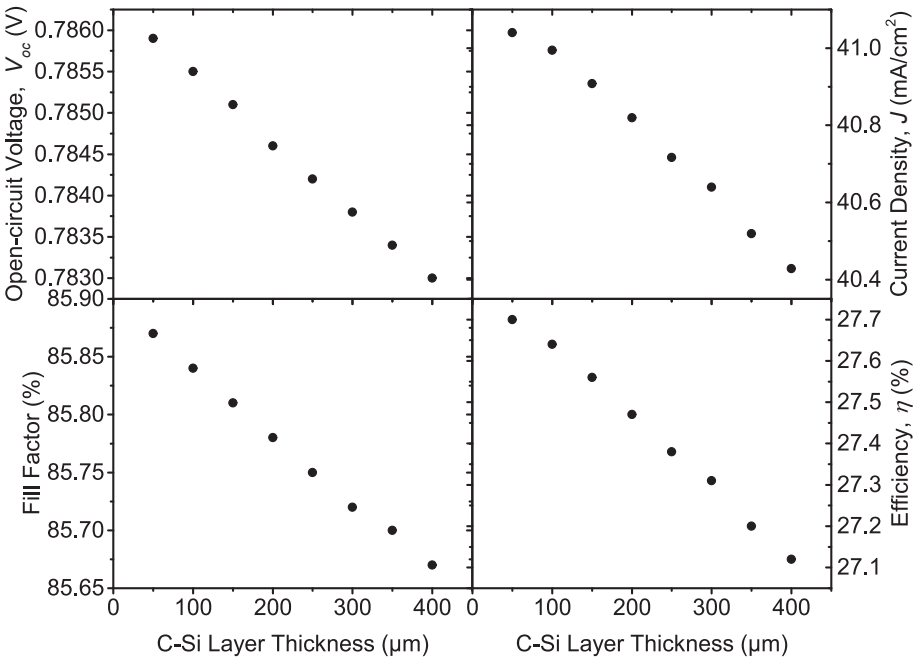

Fig. 12. Effect of Silicon c-Si (p) thickness variation in $Cs_{1-x}Rb_xSnI_3$ perovskite- Silicon Tandem Solar Cell.

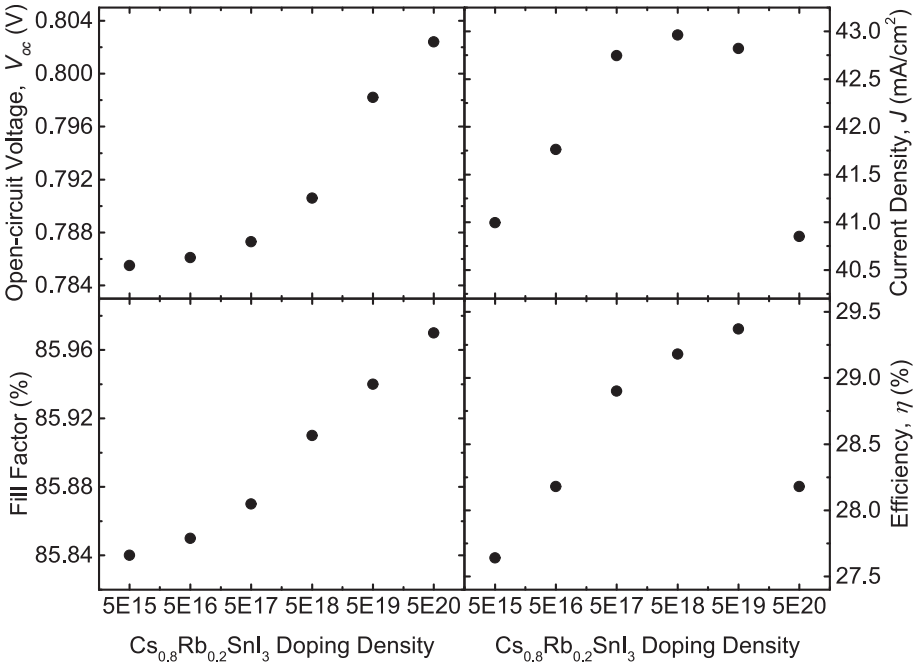

Fig. 13. Doping concentration (N_D) of perovskite Absorber layer in $Cs_{1-x}Rb_xSnI_3$ perovskite- Silicon Tandem Solar Cell.

generated from photons and increase in the in built voltage, V_{bi} due to increase of the photocurrent hence necessitating decrease in J_{sc}. The V_{oc} increases with doping because the shift of the fermi level toward the band edges thereby increasing the contact difference of potential in p-n homojunctions. Increases in FF are due to the decrease in series resistance following the introduction of majority carriers. The slight increase in the PCE of device with active layer can be attributed photo-generated electrons and holes being separated effectively (Guo et al., 2021). Doping levels in the absorber layer influences the defect density and hence device performance and quality of film in a solar cell deteriorate with further increased doping. Optimum doping concentration of the silicon absorber layer was determined at 5×10^{16} cm^{-3}.

3.2.5. *Effect of defect density of perovskite layer in $Cs_{1-x}Rb_xSnI_3$ perovskite-silicon tandem solar cell*

The perovskite absorber layer defect density is varied from 10^{12} cm^{-3} to 10^{16} cm^{-3} to study its influence on the tandem device performance. In Fig. 15, the electrical performance of all the parameters are strongly affected. The J_{sc}, V_{oc}, FF and PCE all decrease with increasing perovskite defect density in the solar cell. The J_{sc} values decreases from 43.32 mA/cm^2 at 10^{12} cm^{-3} to 31.93 mA/cm^2 at 10^{16} cm^{-3}. The V_{oc} values decrease from 0.7869 V to 0.7793 V with increasing defect density. The FF values decrease from 85.86 % to 85.72 % with increasing defect density. The PCE values decrease from 29.27 % to 21.33 % with increasing defect density. Optimum perovskite defect

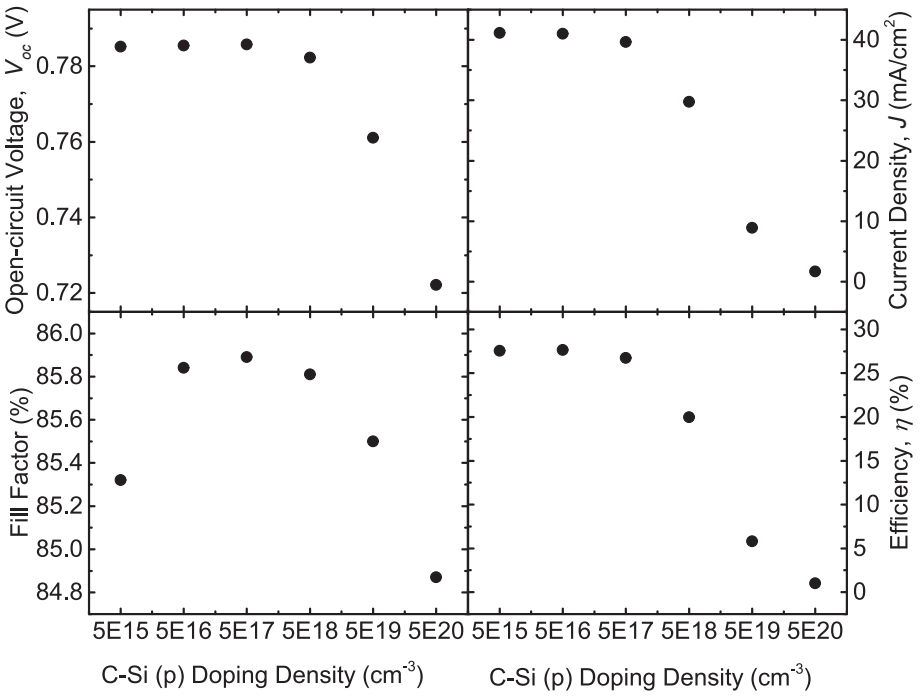

Fig. 14. Doping concentration (N_D) of Silicon Absorber layer in $Cs_{1-x}Rb_xSnI_3$ perovskite- Silicon Tandem Solar Cell.

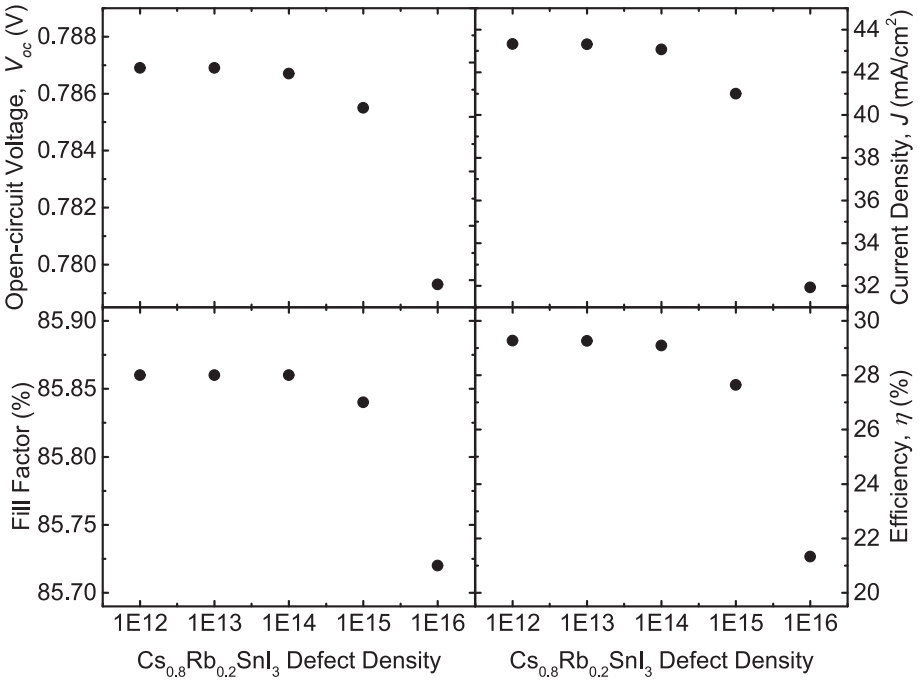

Fig. 15. Effect of defect density of perovskite layer in $Cs_{1-X}Rb_XSnI_3$ perovskite- Silicon Tandem Solar Cell.

density is 1×10^{13} to achieve a more realistic cell. Minority carrier lifespan and mobility both decrease with an increase in defect density, resulting in a reduction in the V_{oc}. The rate of recombination to carrier generation of charge carriers increases hence the reduction in J_{sc} which decrease the device's effectiveness and output over time (Hussain et al., 2021).

3.2.6. Effect of defect density of silicon in $Cs_{1-x}Rb_xSnI_3$ perovskite- silicon tandem solar cell

Defects originate from either added impurities or crystallographic defects such as vacancies or dislocations. The more defects a material has, the less the photocurrent of the solar cell due to increased recombination centers reducing the minority carrier lifetime. The effect of varying the C- Si (p) absorber layer defect density in the $Cs_{1-x}Rb_xSnI_3$ perovskite- Silicon Tandem Solar Cell is investigated as shown in Fig. 16. The silicon absorber layer defect density is varied from 10^{12} cm^{-3} to 10^{16} cm^{-3}. The J_{sc} values decreases from 40.99 mA/cm^2 at 1×10^{12} cm^{-3} to 11.49 mA/cm^2 at 1×10^{16} cm^{-3}. The V_{oc} values decrease from 0.79 V at 1×10^{12} cm^{-3} to 0.61 V at 1×10^{16} cm^{-3} with increasing defect density. The FF values decrease from 85.84 % at 1×10^{12} cm^{-3} to

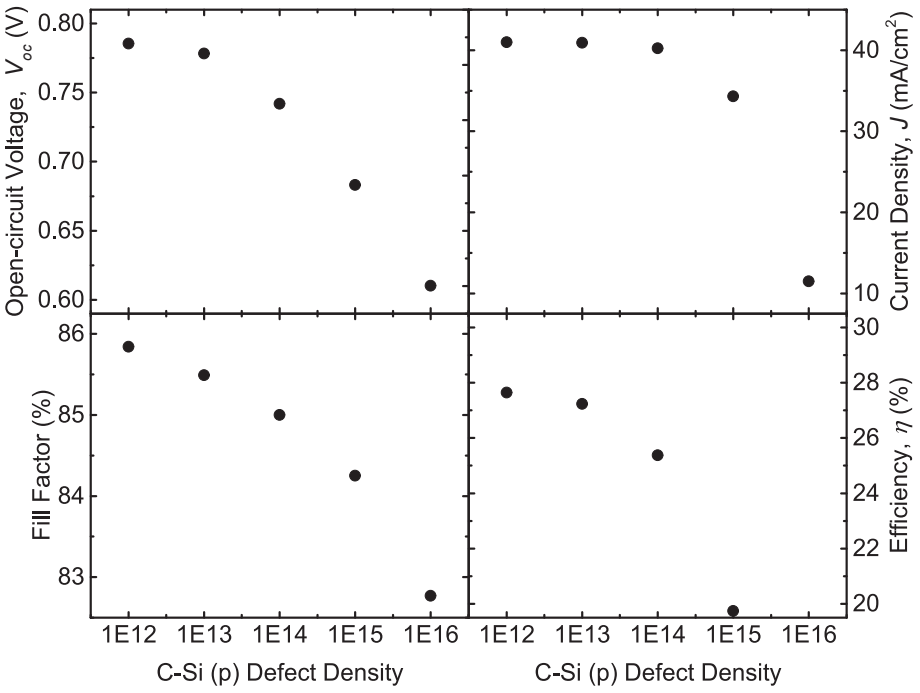

Fig. 16. Effect of defect density of Silicon in $Cs_{1-x}Rb_xSnI_3$ perovskite- Silicon Tandem Solar Cell.

82.77% at 1×10^{16} cm^{-3} with increasing defect density. The PCE values decrease from 27.64 % at 1×10^{12} cm^{-3} to 5.80 % at 1×10^{16} cm^{-3} with increasing defect density. Optimum silicon absorber defect density is determined at 1×10^{12} cm^{-3}. Device performance declines when defect density rises because of an increased rate of recombination, which causes greater scattering and shorter diffusion length (Nalianya et al., 2021).

Optimum values in this study (Table 7), results (Table 8) and J-V spectra (Fig. 17) are as below. Simulation results show optimized absorber thickness and defect and doping densities, ETL thickness, doping densities and CBO and front contact of $Cs_{1-x}Rb_xSnI_3$ perovskite lead to high efficiencies. High efficiency was also achieved by optimizing the thickness, doping densities and defect densities of both the $Cs_{1-x}Rb_xSnI_3$ and C- Si (p) absorber layers in the $Cs_{1-x}Rb_xSnI_3$ perovskite-Silicon tandem solar cell.

Table 7
Optimized parameters for the simulations.

Cell		$Cs_{1-x}Rb_xSnI_3$ Perovskite	Tandem Solar Cell	
			Top Cell	Bottom Cell
Absorber	Thickness	200 nm	100 nm	200 μm
	Doping Density	5 x10^{15}	5 × 10^{19}	5 × 10^{16}
	Defect Density	1×10^{15}	1×10^{14}	1×10^{12}
ETL	Thickness	100 nm		
	Doping Density	1×10^{21}		
	CBO	+ 0.22 eV		
Work Function of ITO Front contact		5.3 eV		

Table 8
Initial and optimized parameters of $Cs_{1-x}Rb_xSnI_3$ Perovskite and $Cs_{1-x}Rb_xSnI_3$ perovskite- Silicon tandem solar cell (*s*).

SOLAR CELL		Open Circuit Voltage, V_{oc} (V)	Short Circuit Current Density, J_{sc} (mA/cm^2)	Fill Factor, FF (%)	Power Conversion Efficiency, PCE (%)
$Cs_{1-x}Rb_xSnI_3$ Perovskite	Initial	0.4757	6.63	65.97	2.08
	Final	1.0356	23.76	83.18	20.46
Crystalline Silicon		0.7400	43.29	83.30	26.68
$Cs_{1-x}Rb_xSnI_3$ perovskite - Silicon tandem	Initial	0.7855	40.99	85.84	27.64
	Final	0.7992	43.39	85.98	29.82

4. Device fabrication

4.1. Perovskite fabrication

ITO coated glass slides will be held in vertical slide holders and ultrasonically swirled in the acetone, highly purified water bath with a few drops of surfactant, high purity deionized water only bath, and thereafter, isopropanol bath. (Marshall et al., 2018)The slides will then be suspended for 15 min, in hot acetone vapour and thereafter UV/O3 treatment for 15 min and immediately transferred into a dry nitrogen filled glovebox for Cs0.8Rb0.2SnI3 film deposition (Marshall et al., 2016), followed by deposition of a PC61BM film and bathocuproine (BCP) respectively by a thermal evaporation pressure of $< 1 \times 10^{-5}$ mbar (with substrate rotation). The Al electrode will be deposited through a shadow mask to make six devices per slide (Marshall et al., 2015).

4.2. Silicon fabrication

All of the Si films utilized in this research will be created by the HWCVD process at a substrate temperature of 150 °C, filament

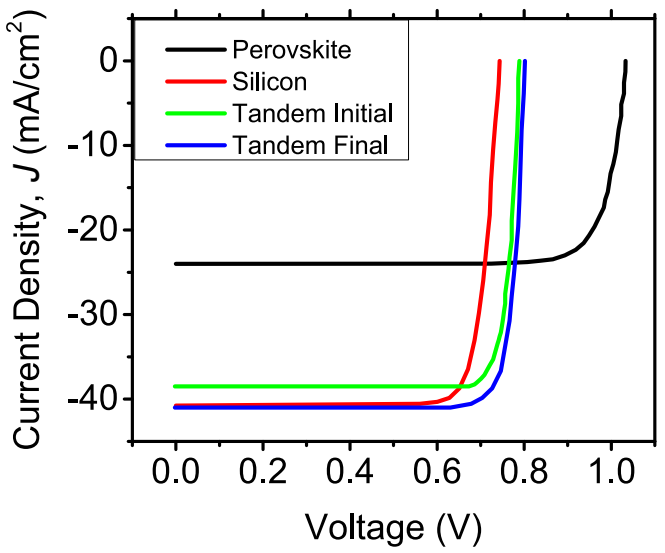

Fig. 17. Optimized and initial JV curves for the perovskite, silicon, initial and final tandem solar cell (s).

temperature of 1700 °C, and total gas flow of 20 sccm and gas pressure of 1 Pa. The doping gas (PH3 for n-type and B2H6 for p-type) concentration Sd = dopant/(dopant + SiH4 + H2) will be maintained between 0.1% and 1%. Prior to the Si film deposition, the c-Si wafers will then be dipped in a 2% HF solution to etch the native surface oxide. The c-Si substrate will thereafter be subjected to the H atom pre-treatment process which is carried out by decomposing H2 through the 1700 °C hot filaments for 10–180 s. The rear surface of the solar cell (Al) and Ag electrodes will be screen printed with aluminum paste and graphite inks respectively.

4.3. Silicon- perovskite tandem Fabrication.

On the fabricated silicon solar cell, just before metallization, a layer of $Cs_{0.8}Rb_{0.2}SnI_3$ prepared from room temperature solutions of RbI, CsI and $SnCl_2$ and tin (II) halide mixed together in 0.8: 0.2: 1: 0.1 M ratio, deposited by spin coating and thereafter, chlorinated ITO deposited by thermal evaporation.

5. Conclusions

This study controllably optimized a lead free $Cs_{0.8}Rb_{0.2}SnI_3$ - silicon tandem solar cell by using Solar cell capacitance simulator (SCAPS ver.3.3.03). Appropriate perovskite cell absorber thickness and low defect density can improve solar power conversion efficiency due to the enhancement of electron - hole generation and low recombination rate. The electron transport layer (PCBM) thickness ensures high carrier concentration and mobility of carriers, doping density ensures effective carrier collection and positive CBO improves perovskite solar cell efficiency. Appropriate carrier doping concentration ensures heightened built-in electric field. Tandem cell provides better utilization of light. The optimum perovskite thickness in the tandem cell ensures maximum exciton dissociation. Doping ensures increase in presence of majority carriers hence built in electric field across the cell. The optimum silicon thickness in the tandem cell ensures efficient charge collection. Optimum doping ensures decreased resistance and increased optical absorption. The low defect density of both the silicon and perovskite layers in the tandem cell reducing the number of trap states where recombination takes place. Optimized work function of the Cl - doped ITO front contact ensures a proper energy alignment in the device. The reassuring power conversion efficiency of 29.82 % is obtained after optimization of all the parameters. The films will be used in generating renewable energy from solar using novel low cost and earth abundant materials.

Declaration of Competing Interest

The authors declare that they have no known competing financial interests or personal relationships that could have appeared to influence the work reported in this paper.

Data availability

Data will be made available on request.

Acknowledgement

This work has greatly been supported by the Department of Electronics and Information Systems (ELIS), University of Gent, Belgium, for providing the SCAPS-1D simulation software through Dr. Marc Burgelman, Kenya Education Network (KENET) mini-grant 2019 to MMUST, Masinde Muliro University of Science and Technology Grant No MMU/URF/2022/1-026 and support from the Partnership for Skills in Applied Sciences, Engineering and Technology (PASET) – Regional Scholarship Innovation Fund (RSIF), Research Grant No. RSIF/RA/005.

References

Agha, D.N.Q., Algwari, Q.T., 2021. The influence of the interface layer between the electron transport layer and absorber on the performance of perovskite solar cells. In: IOP Conf. Ser. Mater. Sci. Eng. IOP Publishing, p. 12033.
Almansouri, I., Ho-Baillie, A., Bremner, S.P., Green, M.A., 2015. Supercharging silicon solar cell performance by means of multijunction concept. IEEE J. Photovoltaics 5 (3), 968–976.
Aman, G., Jahangir, K., Usman, Y., Ghazi, E., Nowsherwan, A., Khizer Jahangir, E., Saleem, M.W., Khalid, M., 2021. Numerical Modeling and Optimization of Perovskite Silicon Tandem Solar Cell Using SCAPS-1D. Sch Bull. 7, 171–184.
Babics, M., De Bastiani, M., Ugur, E., Xu, L., Bristow, H., Toniolo, F., Raja, W., Subbiah, A.S., Liu, J., Torres Merino, L.V., Aydin, E., Sarwade, S., Allen, T.G., Razzaq, A., Wehbe, N., Salvador, M.F., De Wolf, S., 2023. One-year outdoor operation of monolithic perovskite/silicon tandem solar cells. Cell Rep. Phys. Sci. 4 (2), 101280.
Bag, A., Radhakrishnan, R., Nekovei, R., Jeyakumar, R., 2020. Effect of absorber layer, hole transport layer thicknesses, and its doping density on the performance of perovskite solar cells by device simulation. Sol. Energy 196, 177–182.
Baloch, A.A.B., Hossain, M.I., Tabet, N., Alharbi, F.H., 2018. Practical efficiency limit of methylammonium lead iodide perovskite (CH3NH3PbI3) solar cells. J. Phys. Chem. Lett. 9 (2), 426–434.
Bremner, S.P., Yi, C., Almansouri, I., Ho-Baillie, A., Green, M.A., 2016. Optimum band gap combinations to make best use of new photovoltaic materials. Sol. Energy 135, 750–757.
Bush, K.A., Manzoor, S., Frohna, K., Yu, Z.J., Raiford, J.A., Palmstrom, A.F., Wang, H.-P., Prasanna, R., Bent, S.F., Holman, Z.C., McGehee, M.D., 2018. Minimizing current and voltage losses to reach 25% efficient monolithic two-terminal perovskite–silicon tandem solar cells. ACS Energy Lett. 3 (9), 2173–2180.
Chen, B.o., Yu, Z., Liu, K., Zheng, X., Liu, Y.e., Shi, J., Spronk, D., Rudd, P.N., Holman, Z., Huang, J., 2019. Grain Engineering for Perovskite/Silicon Monolithic Tandem Solar Cells with Efficiency of 25.4%. Joule 3 (1), 177–190.
Cheng, Y., Ding, L., 2021. Perovskite/Si tandem solar cells: Fundamentals, advances, challenges, and novel applications. SusMat. 1, 324–344.
Duan, L., Zhang, Y., Yi, H., Haque, F., Deng, R., Guan, H., Zou, Y., Uddin, A., 2020. Trade-off between exciton dissociation and carrier recombination and dielectric properties in Y6-sensitized nonfullerene ternary organic solar cells. Energy Technol. 8, 1900924.
Fazal, M.A., Rubaiee, S., 2023. Progress of PV cell technology: Feasibility of building materials, cost, performance, and stability. Sol. Energy 258, 203–219.
Gan, Y., Bi, X., Liu, Y., Qin, B., Li, Q., Jiang, Q., Mo, P., 2020. Numerical investigation energy conversion performance of tin-based perovskite solar cells using cell capacitance simulator. Energies 13, 5907.
Guo, R., Zhao, Y., Zhang, Y., Deng, Q., Shen, Y., Zhang, W., Shao, G., 2021. Significant performance enhancement of all-inorganic CsPbBr 3 perovskite solar cells enabled by Nb-doped SnO2 as effective electron transport layer. Energy Environ. Mater. 4 (4), 671–680.
Hao, L., Li, T., Ma, X., Wu, J., Qiao, L., Wu, X., Hou, G., Pei, H., Wang, X., Zhang, X., 2021. A tin-based perovskite solar cell with an inverted hole-free transport layer to achieve high energy conversion efficiency by SCAPS device simulation. Opt. Quant. Electron. 53, 1–17.
Hussain, S.S., Riaz, S., Nowsherwan, G.A., Jahangir, K., Raza, A., Iqbal, M.J., Sadiq, I., Hussain, S.M., Naseem, S., Mondol, J., 2021. Numerical modeling and optimization of lead-free hybrid double perovskite solar cell by using SCAPS-1D. J. Renew. Energy. 2021, 1–12.

K. Jäger, M. Jošt, J. Sutter, P. Tockhorn, E. Köhnen, D. Eisenhauer, P. Manley, S. Albrecht, C. Becker, Improving Monolithic Perovskite/Silicon Tandem Solar Cells From an Optical Viewpoint, in: Opt. Devices Mater. Sol. Energy Solid-State Light., Optical Society of America, 2019: pp. PM4C-2.

Jahangir, K., Usman, Y., Ghazi, E., Nowsherwan, A., Khizer Jahangir, E., Saleem, M.W., Khalid, M., 2021. Numerical Modeling and Optimization of Perovskite Silicon Tandem Solar Cell Using SCAPS-1D. Sch. Bull. 7, 171–184.

Jayan, K.D., 2023. Complete modelling and simulation of all perovskite tandem solar cells. Mater. Sci. Eng. B 294, 116506.

Köhnen, E., Jošt, M., Morales-Vilches, A.B., Tockhorn, P., Al-Ashouri, A., Macco, B., Kegelmann, L., Korte, L., Rech, B., Schlatmann, R., Stannowski, B., Albrecht, S., 2019. Highly efficient monolithic perovskite silicon tandem solar cells: analyzing the influence of current mismatch on device performance, Sustain. Energy Fuels 3 (8), 1995–2005.

Li, C., Wang, X., Bi, E., Jiang, F., Park, S.M., Li, Y., Chen, L., Wang, Z., Zeng, L., Chen, H., Liu, Y., Grice, C.R., Abudulimu, A., Chung, J., Xian, Y., Zhu, T., Lai, H., Chen, B., Ellingson, R.J., Fu, F., Ginger, D.S., Song, Z., Sargent, E.H., Yan, Y., 2023. Rational design of Lewis base molecules for stable and efficient inverted perovskite solar cells. Science 379 (6633), 690–694.

Lin, S., Zhang, B., Lü, T.-Y., Zheng, J.-C., Pan, H., Chen, H., Lin, C., Li, X., Zhou, J., 2021. Inorganic Lead-Free B-γ-CsSnI3 Perovskite Solar Cells Using Diverse Electron-Transporting Materials: A Simulation Study. ACS Omega 6 (40), 26689–26698.

Mandadapu, U., Vedanayakam, S.V., Thyagarajan, K., 2017. Simulation and analysis of lead based perovskite solar cell using SCAPS-1D, Indian. J. Sci. Technol. 10, 65–72.

Marshall, K.P., Walton, R.I., Hatton, R.A., 2015. Tin perovskite/fullerene planar layer photovoltaics: improving the efficiency and stability of lead-free devices. J. Mater. Chem. A 3, 11631–11640.

Marshall, K.P., Walker, M., Walton, R.I., Hatton, R.A., 2016. Enhanced stability and efficiency in hole-transport-layer-free CsSnI3 perovskite photovoltaics. Nat. Energy 1, 1–9.

Marshall, K.P., Tao, S., Walker, M., Cook, D.S., Lloyd-Hughes, J., Varagnolo, S., Wijesekara, A., Walker, D., Walton, R.I., Hatton, R.A., 2018. Cs 1–x Rb x SnI 3 light harvesting semiconductors for perovskite photovoltaics. Mater. Chem. Front. 2 (8), 1515–1522.

Mazzarella, L., Lin, Y., Kirner, S., Morales-Vilches, A.B., Korte, L., Albrecht, S., Crossland, E., Stannowski, B., Case, C., Snaith, H.J., 2019. Infrared light management using a nanocrystalline silicon oxide interlayer in monolithic perovskite/silicon heterojunction tandem solar cells with efficiency above 25%. Adv. Energy Mater. 9, 1803241.

Melas-Kyriazi, J., Ding, I.-K., Marchioro, A., Punzi, A., Hardin, B.E., Burkhard, G.F., Tétreault, N., Grätzel, M., Moser, J.-E., McGehee, M.D., 2011. The Effect of Hole Transport Material Pore Filling on Photovoltaic Performance in Solid-State Dye-Sensitized Solar Cells. Adv. Energy Mater. 1 (3), 407–414.

Minemoto, T., Murata, M., 2015. Theoretical analysis on effect of band offsets in perovskite solar cells. Sol. Energy Mater. Sol. Cells 133, 8–14.

Moiz, S.A., Alahmadi, A.N.M., 2021. Design of dopant and lead-free novel perovskite solar cell for 16.85% efficiency. Polymers (Basel) 13, 2110.

Momblona, C., Malinkiewicz, O., Roldán-Carmona, C., Soriano, A., Gil-Escrig, L., Bandiello, E., Scheepers, M., Edri, E., Bolink, H.J., 2014. Efficient methylammonium lead iodide perovskite solar cells with active layers from 300 to 900 nm. APL Mater. 2, 81504.

Nalianya, M.A., Awino, C., Barasa, H., Odari, V., Gaitho, F., Omogo, B., Mageto, M., 2021. Numerical study of lead free CsSn0. 5Ge0. 5I3 perovskite solar cell by SCAPS-1D. Optik (Stuttg) 248, 168060.

Noel, N.K., Stranks, S.D., Abate, A., Wehrenfennig, C., Guarnera, S., Haghighirad, A.-A., Sadhanala, A., Eperon, G.E., Pathak, S.K., Johnston, M.B., Petrozza, A., Herz, L.M., Snaith, H.J., 2014. Lead-free organic–inorganic tin halide perovskites for photovoltaic applications. Energ. Environ. Sci. 7 (9), 3061–3068.

Nogay, G., Sahli, F., Werner, J., Monnard, R., Boccard, M., Despeisse, M., Haug, F.-J., Jeangros, Q., Ingenito, A., Ballif, C., 2019. 25.1%-efficient monolithic perovskite/silicon tandem solar cell based on ap-type monocrystalline textured silicon wafer and high-temperature passivating contacts. ACS Energy Lett. 4 (4), 844–845.

L.D. Partain, M.S. Kuryla, R.E. Weiss, R.A. Ransom, P.S. McLeod, L.M. Fraas, J.A. Cape, 26.1% solar cell efficiency for Ge mechanically stacked under GaAs, J. Appl. Phys. 62 (1987) 3010–3015.

M.S. Rahman, S. Miah, M.S.W. Marma, M. Ibrahim, Numerical Simulation of CsSnI 3-based Perovskite Solar Cells: Influence of doped-ITO Front Contact, in: 2020 IEEE Reg. 10 Conf., IEEE, 2020: pp. 140–145.

S. Rai, B.K. Pandey, D.K. Dwivedi, Device simulation of low cost HTM free perovskite solar cell based on TiO2 electron transport layer, in: AIP Conf. Proc., AIP Publishing LLC, 2020: p. 140022.

Richter, A., Benick, J., Feldmann, F., Fell, A., Hermle, M., Glunz, S.W., 2017. n-Type Si solar cells with passivating electron contact: Identifying sources for efficiency limitations by wafer thickness and resistivity variation. Sol. Energy Mater. Sol. Cells 173, 96–105.

Ruiz-Preciado, M.A., Gota, F., Fassl, P., Hossain, I.M., Singh, R., Laufer, F., Schackmar, F., Feeney, T., Farag, A., Allegro, I., Hu, H., Gharibzadeh, S., Nejand, B.A., Gevaerts, V. S., Simor, M., Bolt, P.J., Paetzold, U.W., 2022. Monolithic Two-Terminal Perovskite/CIS Tandem Solar Cells with Efficiency Approaching 25%. ACS Energy Lett. 7 (7), 2273–2281.

T. Saga, NPG Asia Materials 2, 96-102 (2010), (2010).

Scharber, M.C., Mühlbacher, D., Koppe, M., Denk, P., Waldauf, C., Heeger, A.J., Brabec, C.J., 2006. Design rules for donors in bulk-heterojunction solar cells—Towards 10% energy-conversion efficiency. Adv. Mater. 18, 789–794.

Schulze, P.S.C., Bett, A.J., Bivour, M., Caprioglio, P., Gerspacher, F.M., Kabaklı, Ö.Ş., Richter, A., Stolterfoht, M., Zhang, Q., Neher, D., 2020. 25.1% High-efficiency monolithic perovskite silicon tandem solar cell with a high bandgap perovskite absorber. Sol. RRL. 4, 2000152.

Stevenson, K.J., Luchkin, S., 2021. Photochemically-Induced Phase Segregation of Mixed Halide Perovskite Solar Cells. Meet. Abstr. MA2021-01 (45), 1809.

Sveinbjörnsson, K., Li, B., Mariotti, S., Jarzembowski, E., Kegelmann, L., Wirtz, A., Frühauf, F., Weihrauch, A., Niemann, R., Korte, L., Fertig, F., Müller, J.W., Albrecht, S., 2022. Monolithic Perovskite/Silicon Tandem Solar Cell with 28.7% Efficiency Using Industrial Silicon Bottom Cells. ACS Energy Lett. 7 (8), 2654–2656.

Wei, J., Xiong, Q., Mahpeykar, S.M., Wang, X., 2016. Numerical study of complementary nanostructures for light trapping in colloidal quantum dot solar cells. Nanomaterials 6, 55.

Wu, B., Zhou, Y., Xing, G., Xu, Q., Garces, H.F., Solanki, A., Goh, T.W., Padture, N.P., Sum, T.C., 2017. Long minority-carrier diffusion length and low surface-recombination velocity in inorganic lead-free CsSnI3 perovskite crystal for solar cells. Adv. Funct. Mater. 27, 1604818.

Yoshikawa, K., Kawasaki, H., Yoshida, W., Irie, T., Konishi, K., Nakano, K., Uto, T., Adachi, D., Kanematsu, M., Uzu, H., 2017. Silicon heterojunction solar cell with interdigitated back contacts for a photoconversion efficiency over 26%. Nat. Energy 2, 1–8.

Zhang, C., Qi, L., Chen, Q., Lv, L., Ning, Y.u., Hu, Y., Hou, Y., Teng, F., 2014. Plasma treatment of ITO cathode to fabricate free electron selective layer in inverted polymer solar cells. J. Mater. Chem. C 2 (41), 8715–8722.

Zhao, Y., Datta, K., Phung, N., Bracesco, A.E.A., Zardetto, V., Paggiaro, G., Liu, H., Fardousi, M., Santbergen, R., Moya, P.P., Han, C., Yang, G., Wang, J., Zhang, D., van Gorkom, B.T., van der Pol, T.P.A., Verhage, M., Wienk, M.M., Kessels, W.M.M., Weeber, A., Zeman, M., Mazzarella, L., Creatore, M., Janssen, R.A.J., Isabella, O., 2023. Optical Simulation-Aided Design and Engineering of Monolithic Perovskite/Silicon Tandem Solar Cells. ACS Appl. Energy Mater. 6 (10), 5217–5229.

Zheng, J., Wang, G., Duan, W., Mahmud, M.A., Yi, H., Xu, C., Lambertz, A., Bremner, S., Ding, K., Huang, S., Ho-Baillie, A.W.Y., 2022. Monolithic Perovskite–Perovskite–Silicon Triple-Junction Tandem Solar Cell with an Efficiency of over 20%. ACS Energy Lett. 7 (9), 3003–3005.

Zhong, Y., Tada, A., Izawa, S., Hashimoto, K., Tajima, K., 2014. Enhancement of VOC without loss of JSC in organic solar cells by modification of donor/acceptor interfaces. Adv. Energy Mater. 4, 1301332.